

## Organ Distribution and Bone Tropism of Cellulose Nanocrystals in Living Mice

Laura Colombo,<sup>†</sup> Luca Zoia,<sup>‡</sup> Martina B. Violatto,<sup>†</sup> Sara Previdi,<sup>†</sup> Laura Talamini,<sup>†</sup> Leopoldo Sitia,<sup>†</sup> Francesco Nicotra,<sup>§</sup> Marco Orlandi,<sup>‡</sup> Mario Salmona,<sup>†</sup> Camilla Recordati,<sup>⊥</sup> Paolo Bigini,<sup>\*,†</sup> and Barbara La Ferla<sup>\*,§</sup>

<sup>†</sup>IRCCS-Istituto di Ricerche Farmacologiche “Mario Negri”, 20156 Milan, Italy

<sup>‡</sup>Department of Earth and Environmental Science, University of Milano-Bicocca, Piazza della Scienza 1, 20126 Milan, Italy <sup>§</sup>Department of Biotechnology and Biosciences, University of Milano-Bicocca, Piazza della Scienza 2, 20126 Milano, Italy <sup>⊥</sup>Mouse and Animal Pathology Laboratory, Fondazione Filarete, Viale Ortles 22/4, 20139 Milano, Italy

**ABSTRACT:** Their physicochemical properties and relatively low cost make cellulose nanocrystals (CNCs) a potential candidate for future large-scale production in many fields including nanomedicine. Prior to a sustained and responsible development as theranostic agents, robust and reliable data concerning their safety, biocompatibility, and tissue distribution should be provided. In the present study, CNCs were extracted from Whatman filters functionalized with a fluorescent dye, and their interaction with living organisms has been thoroughly assessed. Our experimental evidence demonstrated that CNCs (1) are well tolerated by healthy mice after systemic injection; (2) are rapidly excreted, thus avoiding bioaccumulation in filter organs such as the kidneys and liver; (3) transiently migrate in bones; and (4) are able to penetrate in the cytoplasm of cancer cells without inducing material-related detrimental effects in terms of cell survival. Our results strongly suggest that the peculiar tropism to the bones is due to the chemical interaction between the  $\text{Ca}^{2+}$  of the bone matrix and the active surface of negatively-charged CNCs. This feature, together with the ability to penetrate cancer cells, makes CNCs a potential nanodevice for theranostics in bone tumors.

Cellulose is the most important natural biopolymer available on Earth. As raw material, it has been used in the form of wood, fibers, and derivatives for a wide spectrum of applications. Its sustainability, renewability, and intrinsic environmental safety make it a preferable natural resource to generate organic materials. Recently, the possibility to obtain cellulose in a defect-free and rod-like crystalline state, called cellulose nanocrystals (CNCs), has opened new methods of exploitation of this material. The procedure is based on the acidic hydrolysis of a wide range of cellulosic substrates, which permits to liberate the high crystalline regions from the disordered domains, leading to the formation of nanometer-sized crystallites.

The CNC width measures approximately a few nanometers, and the length might vary from tens of nanometers to several micrometers depending on the cellulose source.<sup>1</sup> It is possible to obtain CNCs of 100–200 nm in length from wood, while cotton gives CNCs that are 100–300 nm long.<sup>1</sup> CNCs can be extracted not only from wood and cotton, but also from a wide range of forest<sup>2,3</sup> and agricultural residues;<sup>4–6</sup> this large range of exploitation allows us to obtain high-value sustainable biomaterials from low-value lignocellulosic biomasses. The extraction procedure exploits mineral acids,<sup>7</sup> in particular sulfuric acid, which react with the surface hydroxyl groups of cellulose to yield negatively charged sulfate esters. This promotes dispersion of the CNCs in water, avoiding flocculation.<sup>8</sup> In the past decade, an even more increasing interest for CNCs in different industrial and commercial areas has emerged. The exploitation of CNCs (or nanowhiskers) may provide great advantages because of their large availability, complete renewability, physicochemical properties (e.g., high surface area, unique morphology, low density, and mechanical strength), and relative low cost of production. In the last years, several procedures of surface derivatization based on the chemical introduction of different functional groups have been described.<sup>9,10</sup> Some of these strategies are specifically devoted to the conjugation of drugs or targeting agents.<sup>11–18</sup>

The tuning of specific physicochemical properties can greatly influence nanoparticle (NP) biodistribution and, consequently, the therapeutic efficacy of nanodrugs. It has been recently demonstrated that the NP shape is crucial in the vascular transport and in the efficiency of NPs adhesion to the target(s).<sup>19</sup> In this context, it has been reported that rod-shaped NPs exhibit higher specificity versus endothelial targets compared with their spherical counterparts,<sup>20</sup> thus allowing a potential use of nanotubes for theranostic purposes.<sup>21</sup> From a pharmacokinetic point of view, it has been observed that once in the bloodstream, spherical NPs remain in the center of the vessels, while NPs with elongated geometric structure flow closer to the endothelial wall. This reduces the risk of NP uptake by monocytes and enhances their extravasation.<sup>22,23</sup>

Even if nanorods have a higher surface/volume ratio and a lower drug loading efficiency compared to the nanospheres, the rod shape may greatly influence the adhesion to specific organs or tissues.<sup>24</sup> In this context, rod-like CNCs may be a very promising theranostic tool in bone disorders.<sup>25–27</sup>

One of the main limitations of the compounds used in bone diseases is the extremely low tropism toward their anatomical target.<sup>28</sup> This issue often requires the use of very high doses of drugs with the consequent risk of inducing systemic adverse effects. Moreover, almost all systemically injected drugs do not directly interact with bones. Therefore, the discovery of carriers able to reach and accumulate in the bones would be crucial to pave the way for the development of targeted therapy in pathologies embracing different areas (tumors, inflammatory disorders, osteoporosis, and rheumatoid arthritis). In a very high percentage of cases, commonly used nanomaterials (e.g., polymeric NPs or nanoliposomes) did not show a specific localization

in bones. This lack of tropism may be in part accounted for physicochemical parameters such as the size, shape, surface functionalization, and external charge, which can greatly influence the interaction with biological matrices of external osteal surface.<sup>29–31</sup> It has been recently reported that a bilayer of bacterial nanocellulose scaffold supports neocartilage formation *in vitro* and *in vivo*<sup>32</sup> and that negatively charged molecules, such as the bisphosphonates, were able to target drugs to bone.<sup>33,34</sup> On the basis of these interesting premises, our project was mainly aimed at evaluating the interaction of negatively charged CNCs with healthy mice, with particular emphasis on the study of bone tropism. To this purpose, a careful evaluation of the biodistribution, accumulation, and clearance in filter organs of CNCs in mice has been extensively considered in our study. To follow the fate of CNCs in living animals at different time points after single administration,<sup>35</sup> a fluorescent dye detectable by *in vivo* optical imaging was covalently linked to the crystals. The presence of the covalent bond ensured us to track only the specific CNCs' signal, which avoids problems due to the biological elution of the dye. This technique was already optimized in a previous study by our group where the same dye in the same experimental models showed a very fast clearance when administrated free or conjugated with small molecules such as the biotin.<sup>36</sup>

## EXPERIMENTAL SECTION

**Materials.** Whatman cellulose filter paper was purchased from Sigma-Aldrich. Alexa Fluor 633 hydrazide, bis(triethylammonium) salt, was purchased from Life Technologies. Dialysis tubes in cellulose membrane with a molecular weight cut-off of 12 000 Da were purchased from Sigma-Aldrich. Dulbecco's Modified Eagle's Medium-high glucose (DMEM 4500 mg/L glucose, with/without L-glutamine, and with/without sodium bicarbonate, without sodium pyruvate, liquid, sterile-filtered, suitable for cell culture, Sigma-Aldrich), fetal bovine serum (FBS, USA origin, sterile-filtered, suitable for cell culture, Sigma-Aldrich), phosphate buffered saline (PBS, 10× concentrate, with/without Ca<sup>2+</sup>/Mg<sup>2+</sup>, BioPerformance Certified, suitable for cell culture, Sigma-Aldrich), ethylenediaminetetraacetic acid (EDTA Sigma-Aldrich), Hoechst-33258 (Hoechst-33258, Penta-hydrate (bis-Benzimide) 10 mg/mL solution in water, Molecular Probes), fluormount (fluormount mounting medium, 25 mL, Bio-Optica), and ketamine hydrochloride solution (1.0 mg/mL in methanol, Sigma-Aldrich) were used.

Preparation of Alexa Fluor 633 Labeled CNCs. CNCs were extracted from Whatman filter paper by acid hydrolysis in 64% H<sub>2</sub>SO<sub>4</sub> for 1 h at 55 °C at acid/cellulose ratio of 10 w/w. After acidic treatment, the content of the flask was poured into 10-fold volume of cold water and stirred. Cellulose sediment was purified by repeated cycles of centrifugation at the acceleration of 3200g for 15 min, and the resuspension of the solid component with distilled water was carried out by ultrasonic mixing for 5 min. After a turbid

supernatant was obtained, the suspension was dialyzed against distilled and ultrapure Milli-Q water for 1 week until pH of 6 was reached. The obtained CNCs have been functionalized according to a modification of the procedure developed by Huang et al.<sup>37</sup> To a suspension of CNCs (0.5%, 25 mL), 1 mg of Alexa Fluor 633 hydrazide, bis-(triethylammonium) salt, and 200  $\mu$ L of acetic acid were added. The mixture was left to react at room temperature in the dark. After 24 h, the mixture was dialyzed against distilled water for 1 week to remove the acetic acid and the unreacted fluorophore. Before all the in vitro, in vivo, and ex-vivo experiments, CNCs were separated from any precipitate by centrifugation at 6000 rpm for 5 min and then sterilized under UV light for at least 1 h.

Characterization of CNCs was performed by UV–vis spectroscopy, atomic force microscopy (AFM) analysis, and dynamic light scattering (DLS) measurements. The UV–vis absorption spectra were collected with a UV–vis spectrophotometer Evolution 300 (Thermo Scientific).<sup>38,39</sup> For AFM analysis, 500  $\mu$ L of sample of the cellulose nanocrystals was diluted with 950  $\mu$ L of distilled water, and 50  $\mu$ L was immediately added onto freshly cleaved mica at room temperature for 5 min: samples were washed and dried under gentle nitrogen flow. AFM analysis was carried out on a Multimode AFM with a Nanoscope V system (Veeco/Digital Instruments, Mannheim, Germany) operating in tapping mode, using standard antimony(n) doped silicon probes (T, 3.5–4.5  $\mu$ m; L, 115–135  $\mu$ m; K, 20–80 N/m) (Bruker Corporation, Billerica, MA) with a scan rate in the 0.5–1.2 Hz range proportionally to the area scanned, and the images were acquired in height and amplitude error. AFM images were analyzed by Scanning Probe Image Processor (SPIP-version-5.1.6, release April 13, 2011) data analysis package. To exclude the interference of possible artifacts, extra control samples, such as freshly cleaved mica and freshly cleaved mica soaked with buffer, were also used. All the topographic patterns and SPIP characterization described were repeated by additional measurements on a minimum of five different, well-separated areas.

DLS and zeta-potential measurements were performed using a Zeta Sizer Nano 3600 (Malvern) with operating laser ( $\lambda = 632.8$  nm) and a backscattering angle of 173°. The zeta potential data were processed by Zetasizer Software 7.03. The samples were prepared by dilution of initial particles of stock solution 7 g/L in Milli-Q water by obtaining the final concentration of 140 mg/L. Measurements were carried out at 25 °C using a disposable cuvette with 10 mm optical path length. Three replicate measurements per sample were performed to establish measurements repeatability.

Cellular Internalization and Cytotoxicity. HeLa cells (ATCC CCL-2; from human cervix adenocarcinoma) were selected as the cellular line model to evaluate the ability of CNCs to be efficiently internalized inside them. Cells were grown in DMEM complemented with 10% FBS, 2 mM L-glutamine, and 100 U penicillin/0.1 mg/mL streptomycin and were maintained at 37 °C in 5% CO<sub>2</sub>. Briefly, cells were seeded at a density of 20 000 cell/well into round glass slides in 24-well plates. After 24 h, culture medium

was removed and replaced with a suspension of CNCs in medium at three different concentrations: 7  $\mu\text{g/mL}$ , 14  $\mu\text{g/mL}$ , and 35  $\mu\text{g/mL}$ . Three different time-points were considered: 6 h, 24 h, and 48 h of incubation. Three replicated wells were used for each concentration, and untreated cells were added as control. After CNCs removal, cells were washed with PBS once and fixed with 4% paraformaldehyde in PBS for 40 min. Then nuclei were stained with Hoechst-33258 (2  $\mu\text{g/mL}$  in PBS) for 40 min. Samples were mounted on glass cover slides with fluormount mounting medium. Cells were analyzed with Olympus Fluoview microscope BX61 (Tokyo, Japan) with confocal system FV500 equipped by specific lasers  $\lambda_{\text{exc}}$  405 nm for Hoechst-33258 and  $\lambda_{\text{exc}}$  635 nm to visualize Alexa Fluor 633 conjugated to CNCs as previously described.<sup>36</sup> As recently reported,<sup>40</sup> the quantification of the mean level of fluorescence for each single cell was carried in HeLa at different time-points (6 h, 24 h, and 48 h) and upon 7  $\mu\text{g/mL}$ , 14  $\mu\text{g/mL}$ , and 35  $\mu\text{g/mL}$  of CNCs by a dedicated software of cell segmentation (Tissue-Quest, TissueGnostic, Wien). The incubation with Alexa Fluor 633 alone was carried out as inner control. Regarding cytotoxicity, HeLa cells (15 000/well) were seeded in quadruplicate in 96-well plates and treated with increasing concentrations of CNCs (14  $\mu\text{g/mL}$ , 37  $\mu\text{g/mL}$ , 70  $\mu\text{g/mL}$ , 140  $\mu\text{g/mL}$ ) for 6, 24, and 48 h. The medium without NPs was added as a control. At the end of the treatment, cell proliferation was determined by MTS assay using Cell Titer 96 Aqueous cell proliferation assay kit (Promega). The optical density of each well was measured by using Infinite 200 microplate reader (Tecan) at 490 nm. The number of living cells was compared in the presence and absence of CNCs.

**In Vivo Analysis.** For in vivo analyses, 3-month-old female NFR mice were used. Animals were bred and maintained under specific pathogen-free conditions in the Institute's Animal Care Facilities; they received food and water ad libitum and were regularly checked by a certified veterinarian who is responsible for animal welfare supervision and experimental protocol revision. Procedures involving animals and their care were conducted in conformity with the institutional guidelines at the IRCCS-Institute for Pharmacological Research "Mario Negri" in compliance with national (Decreto Legge nr 116/ 92, Gazzetta Ufficiale, supplement 40, February 18, 1992; Circolare nr 8, Gazzetta Ufficiale, July 14, 1994) and international laws and policies (EEC Council Directive 86/609, OJL 358, 1, Dec. 12, 1987; Guide for the Care and Use of Laboratory Animals, U.S. National Research Council, eighth edition, 2011). This project of research has been reviewed by IRCCS-IRFMN Animal Care and Use Committee (IACUC) and then approved by the Italian "IstitutoSuperiore di Sanita"(code: 17/01 D Appl 3). A suspension of CNC NPs, in 120  $\mu\text{L}$  of sterile PBS at a concentration of 35  $\mu\text{g/mL}$ , was injected in the tail vein. Vehicle-treated animals received the same volume of sterile PBS without NPs. For in vivo studies, optical imaging was conducted on animals before and at 1 h, 24 h, and 7 days after CNCs injection using Explore Optix System (ART, Advanced Research Technologies, Montreal, Canada), as already described by our group.<sup>36</sup> Selected region

of interest (ROI) scan (ventral whole body, tail, and hind leg) was performed with a step size of 2 mm. At the end of each scanning, animals were placed in their cage; no sufferance or stress was recorded during the whole duration of the experiments.

**Ex Vivo Analysis.** For each time point, three mice, randomly selected before the study, were sacrificed 1 h, 24 h, and 7 days after CNCs injection by an overdose of ketamine (150 mg/kg) and medetomidine (2 mg/kg). To ensure optimal quality of tissues for histological analysis and to remove the blood from tissues, intracardial perfusion with a solution of paraformaldehyde 4% dissolved in PBS (10 mL/g mouse) was carried out, as previously described by our group.<sup>41</sup> For histological evaluation, liver, spleen, and kidneys were frozen. Histological analyses were performed by incubating cryostat serial sections (30  $\mu\text{m}$  of thickness) with the vital nuclear dye Hoechst-33258 (2  $\mu\text{g}/\text{mL}$  in PBS) and then visualized by Olympus Fluoview microscope BX61 (Tokyo, Japan) with confocal system FV500 equipped by specific lasers  $\lambda_{\text{exc}} = 405 \text{ nm}$  for Hoechst-33258 and  $\lambda_{\text{exc}} = 635 \text{ nm}$  to visualize the specific signal associated with CNCs. The quantification of CNC accumulation was calculated as percentage of red spots in five randomly selected sections from liver, spleen, and kidneys at the time points corresponding to the sacrifice of animals (10 fields for each sections, the sampling field was  $265 \mu\text{m} \times 178.7 \mu\text{m}$  for each rectangle). This postprocessing of images was carried out through a specific software (Tissue-Quest, TissueGnostic, Wien). To further evaluate the specific localization of the signal to the limb bones suggested by in vivo optical imaging, femurs, tibias, and the distal part of hind limbs were collected and scanned by an automated scanner that produces digital images of fluorescent samples (Typhoon, GE Healthcare, Fairfield, CT). The measurements of the signal revealed using the red 633 laser were processed by Image-J (NIH) with a gray-level scale. At the end, to understand if the CNCs actually interacted with the  $\text{Ca}^{2+}$  localized in the bone matrix, another scanning was carried out by comparing the signals from bones previously incubated with the  $\text{Ca}^{2+}$  chelator EDTA or in PBS, respectively.

**Data Calculation and Statistical Analysis.** All data were expressed as mean  $\pm$  standard deviation (SD). One-way analysis of variance (ANOVA), followed by Bonferroni's post-test analysis, was used. All statistical analyses were done using the GraphPad Prism version 6.00 for Windows (Graph-Pad Software, San Diego, CA).

## **RESULTS AND DISCUSSION**

**Design and Characterization of Fluorescently Labeled CNCs.** CNCs have been extracted from Whatman filter paper by a methodology based on the sulfuric acid hydrolysis reaction.<sup>1</sup> The procedure permitted to isolate a slightly turbid stable aqueous suspension (0.5% w/w consistency) of rod-like CNCs. For this study, as fluorophore hydrazine derivative, we used the Alexa Fluor 633 hydrazide

bis(triethylammonium) because of its high polarity (and consequently high water solubility), high photostability, high absorptivity, and high fluorescence quantum yield. An extensive dialysis time was applied to remove the unreacted and not covalently bound Alexa Fluor 633 from the brightly blue CNCs suspension. The Alexa Fluor633 content on CNCs was determined by UV–vis spectroscopy. Figure 1 (lower panel) shows the UV–vis absorption spectra in pure water (pH 7.0) of Alexa Fluor 633 labeled CNCs with the spectra of unlabeled ones. The spectrum of the Alexa Fluor 633 labeled CNCs (dot line) showed maxima peaks at 560 and 630 nm, consistent with the data reported in the specifications. Unlabeled CNCs (black line) did not show any specific absorption peaks in the wavelength range from 250–800 nm, with only an increasing trend in absorbance at lower wavelengths.

Using the given absorption intensities ( $100\,000\text{ cm}^{-1}\text{ M}^{-1}$ ), we calculated an Alexa Fluor 633 (MW 1142 g/mol) content of  $7\text{ }\mu\text{mol/g}$  of CNCs. The corresponding degree of substitution (DS) based on the dye content per anhydroglucose unit (AGU) (MW 162 g/mol) has been calculated  $\text{DS} = 0.0011$ . The DS value is quite low, in fact it corresponds to approximately 1 molecule of dye per 1000 AGU, but it is consistent with the limited number of accessible reaction sites (the terminal hemiacetal groups) and with steric hindrance considerations. The degree of substitution of the AGU at the end of cellulose nanocrystals ( $\text{DS}_{\text{end}}$ ) has been calculated by the formula  $\text{DS}_{\text{end}} = \text{DS} \times (420\,000/1200)$ . The formula is based on the assumption of a model CNC 20 nm wide and 200 nm long. If the length of a glucan chain is approximately 0.57 nm, the CNC model is roughly  $35 \times 35 \times 3500$  AGU, with a total of 420 000 AGU and about 1200 AGU in the cross-section.  $\text{DS}_{\text{end}}$  was found to be 0.38, suggesting that one in three of the reducing end groups has reacted with the dye.<sup>10</sup> The CNCs surface is characterized by the presence of different hydroxyl groups of cellulose and negatively charged sulfate esters groups introduced during the extraction.<sup>24</sup> We performed DLS measurements, and we found a  $\zeta$ -potential of  $-39.0 \pm 1.0$  mV, a dimension of  $92.4 \pm 1.8$  nm (before functionalization), a  $\zeta$ -potential of  $-40.6 \pm 1.3$  mV, and a dimension of  $105.0 \pm 6.1$  after functionalization, in agreement with the literature.<sup>42</sup> The small variation in DLS measurement and the low DS value indicate that the active surface of CNCs has been preserved during the functionalization. It is therefore possible to hypothesize that both the chemical surface properties and the morphological ones could be important in determining the tropism behavior.<sup>36,43,44</sup> The process we followed during functionalization helped us to minimize the modification of the unique morphological properties and to maintain the original chemical surface activity of CNCs. Briefly, the reaction between the reducing end-group of the terminal AGU of the  $\beta(1 \rightarrow 4)$  polysaccharide cellulose chains with an hydrazo group of the fluorophore was performed. Although amines have been extensively utilized to modify reducing sugars, the most reactive reagents for forming stable conjugates of aldehydes and ketones are usually hydrazine derivative. The reaction for incorporating hydrazine derivative of methylcumarin in CNCs has been recently reported.<sup>10</sup> The hemiacetal

group on the anomeric carbon (in the open aldehydic form) readily reacts with the hydrazine in mild aqueous conditions to form the corresponding stable glycosyl-hydrazine, as reported in Figure 1 (upper panel).

The effectiveness of the purification process, the homogeneity, and the polydispersity of CNCs were assessed by TEM (data not shown) and AFM (Figure 2A), showing the typical rod-like morphology and the absence of debris. Regarding the colloidal integrity (pivotal in NP biomedical applications), the obtained CNCs suspension was stable over a period of weeks, and after 1 month at 4 °C in the dark, the precipitation of solids was not observed. Moreover, the DLS measurements after this period of conservation were the same as fresh-prepared suspension (data not reported). This is likely due to the presence of sulfate ester functional groups on the CNCs surface that stabilize the colloidal suspension, and the addition of specific surfactants, usually utilized for other nanoparticles stabilization (i.e., PEGs), was not necessary.

Further TEM analysis (data not shown) revealed that CNCs modified with Alexa Fluor 633 maintain the typical rod-like morphology characterized by filamentary structures with a length in the range of 200–300 nm and a width of 7–10 nm. As reported in Figure 2, panel A, AFM analysis confirmed that the sample contained rod-like structures with a thickness in the range of 7–10 nm and height in the range of 5–20 nm (Figure 2B). Moreover, two main particle length distributions were observed: 100–150 (~60%) and 200–350 nm (~40%).

Once demonstrated that the basal stability features of the particles were not affected by the functionalization with the dye, the interaction of fluorescent CNCs with biological matrices was evaluated at increasing steps of complexity. At first, the potential ability of internalization in cells was assessed by incubating CNCs in HeLa cells upon different concentrations and for different intervals of time. HeLa cells were selected because of the extensive characterization already available in literature about the kinetics of internalization of a wide range of nanocarriers in this cell line.

Previous studies have shown that surface charge both influenced the cellular uptake and the cytotoxicity of fluorescently labeled CNCs and that no significant internalization of negatively charged CNC-FITC in human embryonic kidney 293 (HEK 293) and *Spodoptera frugiperda* (Sf9) was observed.<sup>48</sup>

The results obtained in our experiments showed no specific signal related to CNCs after 6 h of incubation (data not shown), while a mild internalization of CNCs was detectable after 24 h of incubation (Figure 3A, left column). The rate of internalization was lower than that observed for other NPs with different physicochemical features.<sup>36,40</sup> This limited uptake could be likely due to the negative  $\zeta$ -potential or the elongated shape: both factors may influence the interaction with cell membrane and the endosomal vesicle formation.<sup>45,47</sup> After 48 h of incubation, CNCs progressively penetrated in cells, with a concentration-dependent manner (Figure 3A, middle column; Figure 3B). The merge between the fluorescent signals and the differential interference contrast (Nomarsky), which enabled us to visualize the

shape of the cells in a 3D-like manner, showed spotted red circles exclusively confined to the cytoplasm. This peculiar spotted staining strongly suggested CNC clustering into endocytic vesicles (Figure 3A, right column). The quantification of the red fluorescence for each single cell confirmed the observational results (Figure 3B). To evaluate if the CNCs entry might produce a toxic effect, a counting of living cells has been carried out by MTS assay. The histogram (Figure 3C) showed that in our study, CNCs internalization did not lead to any cytotoxic effect, at least at different exposure times and up to concentrations 10-fold higher than those reported in our images. As expected, the incubation with the fluorescent dye alone did not show any signal inside HeLa cells. We used this kind of dye because of its inability to pass through living cells at the basal condition.<sup>49</sup> The penetration of this dye needs, in fact, procedures such as electroporation<sup>50</sup> or intracellular injection in neurons.<sup>51</sup> The other strong advantage of using a fluorophore emitting in the infrared region is that tissue autofluorescence is extremely low at high wavelengths, thus improving the specific traceability of the dye during imaging experiments.

To deeper characterize the potential of neo-synthesized CNCs as future vectors for drug delivery, analyses in living animals were carried out. A solution of 120  $\mu$ L of CNCs [3.5  $\mu$ g/mL] was intravenously administrated in healthy mice, and the main kinetic parameters (e.g., biodistribution, bioaccumulation, clearance) were examined by a combined strategy coupling noninvasive in vivo imaging analysis to ex vivo studies. A longitudinal pattern of CNC biodistribution is shown in Figure 4. One hour after CNCs administration, a strong signal was found in the mid and cranial portions of the abdomen, likely localized at level of the liver and kidneys with a weaker fluorescence in correspondence to the pelvic region (likely related to the urinary bladder). The signal associated with the liver (right side of epigastric region) was markedly reduced 24 h after CNC administration, while it was almost absent at the last time-point (7 days). On the contrary, the signal localized in the left epigastric region, already evident 1 h after CNC administration, was also detected up until 7 days. This effect is likely due to the migration of blood cells to the spleen after CNC-uptake in the bloodstream. The rapid clearance through the excretory systems and the slower reduction from spleen are not surprising and are somehow similar to those observed for many other contrast agents. This difference is mainly related to the fact that the complete metabolism and elimination of blood cells by spleen requires a longer time in comparison to the clearance through feces and urine.

At 24 h, a strong signal appeared behind the liver region, and after 7 days, it was localized in the central part of the abdomen, likely overlapping the intestinal tract, and possibly suggesting a progressive accumulation of CNCs in the cecal content and therefore suggesting an efficient clearance of the CNCs. A strong signal was found in the tail vein (the site of CNCs injection) up to 24 h after the administration. Very interestingly, the scanning at level of the distal portion of the left hind limb revealed the presence of CNCs-related signal; this particular localization was observed neither using polymeric nanoparticles<sup>40</sup> nor avidin

nucleic-acid nanoassemblies.<sup>36</sup> It is important to underline that the lack of signal in the forelegs is merely related to the choice of region of interest for the scanning (here we focused the attention on the hind legs) and not by an exclusively tropism to the posterior region of the animal body. In a previous study, we found that the signal associated with the low molecular weight biotin–fluorophore complex very rapidly disappeared from the whole body by fast renal filtration and excretion; this result strongly suggests that the presence of signal in mice, showed in Figure 4, was directly related to the association between CNC and the dye.<sup>36</sup>

Histological analysis (Figure 5A) confirmed the different temporal pattern of CNC biodistribution between liver (upper panels), kidneys (middle panels), and spleen (lower panels). The quantitative results reported in Figure 5, panel B confirmed the observational results. In both liver and kidneys, an early migration of CNCs to the parenchyma was followed by a rapid clearance before the first week after the administration. This result indicates that an early excretion of CNCs occurred both via biliary and urinary routes, supporting the results of the *in vivo* imaging where the CNC signal was detected in correspondence of the urinary bladder and intestinal tract. Regarding the CNC intraorgan distribution in liver and kidneys, images seem to suggest an early uptake by hepatocytes and renal tubular epithelial cells. Very interestingly, the biodistribution of CNCs in the spleen followed an opposite fate. A progressive increase of the signal was in fact observed in the red pulp of CNCs-treated mice. However, this is a typical processes of splenic catabolism of blood cells or different NPs<sup>52,53</sup> at this time-point. Our study, which was stopped at 7 days after administration, did not show any evidence of toxicity that could make us exclude a major concern after single administration of CNCs in mice. This suggests a slower but progressive accumulation of CNCs by splenic macrophages as compared to the faster uptake and clearance by hepatocytes and renal tubules. Overall, the rapid excretion by filter organs is in accordance with the high biocompatibility of this material and also strengthens the potential development as theranostic tool. All these features make this kind of material a potential diagnostic agent and also suggest the future conjugation with drugs to be considered as a therapeutic agent. The ability of CNCs to enter in cancer cells further supports this latter hypothesis, in particular in the field of bone metastases.

*In vivo* optical imaging revealed a CNC-related signal corresponding to the hind limbs (Figure 4, lower panel). To verify if this signal was actually associated with the bone tissue, *ex vivo* analyses were carried out. Figure 6, panel A shows representative images of fluorescence scanning of femurs, tibias, and distal hind leg. A noticeable increase of the dark staining associated with the wavelength of the Alexa Fluor 633 dye was present in all examined bones from treated mice already at 1 h after CNCs administration. The signal intensity progressively decreased over time, as previously observed by *in vivo* imaging. A significant but transient increase of the Alexa Fluor 633 related signal in femurs and distal hind leg of CNC-treated

mice was found by quantitative analysis (Figure 6B, left and right diagrams, respectively). A trend of increase was also observed comparing tibias from untreated and CNC-treated mice (Figure 6B, middle panel). On the basis of these data, we hypothesized that negatively-charged CNCs interact with the  $\text{Ca}^{2+}$  ions contained in the bone matrix and this interaction was the reason for this transient signal. To verify this hypothesis, few samples of femurs and tibias were decalcified with the  $\text{Ca}^{2+}$  chelator (EDTA) and analyzed by fluorescence scanning. The drastic breakdown of CNC-related signal in decalcified bones EDTA (Figure 6C, right diagram) strongly supported the hypothesis that a transient and specific electrostatic interaction between CNCs and bone matrix occurs in treated mice.

## CONCLUSIONS

The present study provides a careful characterization of CNCs from their extraction to their interaction with living rodents. In this study, the interaction between CNCs and biological matrices has been investigated at increasing level of complexity, and it has been enabled by a specific conjugation with a vital dye mimicking a diagnostic reporter. The main outcomes emerging from this study are that (i) fluorescently labeled CNCs are stable to be easily detectable in the body of healthy immunocompetent mice and biocompatible to hypothesize an approach as diagnostic tracers; (ii) CNCs have a peculiar and transient tropism to the limb bones that is likely related to the interaction with the  $\text{Ca}^{2+}$  deposits in the bone matrix; and (iii) negatively-charged CNCs showed a slow but evident internalization in cells without compromising their survival.

The functionalization method adopted does not involve the use of organic solvents and exploits a prolonged dialysis in ultrapure Milli-Q water, which guarantees the removal of any contaminant. For the derivatization with the Alexa Fluor 633 fluorophore, the reducing end-group of the terminal glucose unit of cellulose chains has been exploited; this method could be extended in a straightforward manner to the conjugation to other chemical entities for theranostic purposes. Along with the hydrazo functional group exploited in this case for the linkage to the fluorophore, other functionalities such as aminoxy group<sup>54,55</sup> or the reductive amination approach, widely used in carbohydrate conjugation protocols, could be applied. More-over, heterobifunctional linkers<sup>56</sup> could be used to present any required functionality for the conjugation of a desired entity, and dendrimeric polyfunctional structures could be exploited to increase loading capacity and to allow a simultaneous introduction of different entities. These may include diagnostic agents such as Gadolinium complexes for MRI, radionuclides chelators for PET, and therapeutic agents.

All these results make CNCs a very promising candidate for potential development in the field of theranostic, in particular toward bone diseases with particular emphasis to bone tumors, as demonstrated by the ability to internalize in cancer cells.

## **AUTHOR INFORMATION**

Corresponding Authors

\*E-mail: paolo.bigini@marionegri.it. Phone: +39-02-39014221.

Fax: +39-0239014744.

\*E-mail: barbara.laferla@unimib.it. Phone: +39-0264483421.

Fax: +39-0264483565.

Author Contributions

L.C. and L.Z. contributed equally to this work. The manuscript was written through contributions of all authors. All authors have given approval to the final version of the manuscript.

Notes

The authors declare no competing financial interest.

## **REFERENCES**

- (1) Habibi, Y.; Lucia, L. A.; Rojas, O. J. Cellulose Nano-Crystals: Chemistry, Self-Assembly, and Applications. *Chem. Rev.* 2010, 110, 3479–500.
- (2) Siqueira, G.; Abdillahi, H.; Bras, J.; Dufresne, A. High reinforcing capability Cellulose Nano-Crystals extracted from *Syngonanthus nitens* (CapimDourado). *Cellulose* 2010, 17, 289–298.
- (3) Sheltami, R. M.; Abdullah, I.; Ahmad, I.; Dufresne, A.; Kargarzadeh, H. Extraction of Cellulose Nano-Crystals from mengkuang leaves (*Pandanus tectorius*). *Carbohydr. Polym.* 2012, 88, 772–779.
- (4) Rosa, S. M. L.; Rehman, N.; de Miranda, M. I. G.; Nachtigall, S. M. B.; Bica, C. L. D. Chlorine-free extraction of Cellulose from rice husk and whisker isolation. *Carbohydr. Polym.* 2012, 87, 1131–1138.
- (5) Johar, N.; Ahmad, I.; Dufresne, A. Extraction, preparation and characterization of Cellulose fibres and Nano-Crystals from rice husk. *Ind. Crops Prod.* 2012, 37, 93–99.

- (6) Lu, P.; Hsieh, Y. L. Preparation and characterization of Cellulose Nano-Crystals from rice straw. *Carbohydr. Polym.* 2012, 87, 564–573.
- (7) Filpponen, I.; Argyropoulos, D. S. Regular Linking of Cellulose Nano-Crystals via Click Chemistry: Synthesis and Formation of Cellulose Nanoplatelet Gels. *Biomacromolecules* 2010, 11, 1060–1066.
- (8) Abitbol, T.; Kloser, E.; Gray, D. G. Estimation of the surface sulfur content of Cellulose Nano-Crystals prepared by sulfuric acid hydrolysis. *Cellulose* 2013, 20, 785–794.
- (9) Eyley, S.; Thielemans, W. Surface modification of Cellulose Nano-Crystals. *Nanoscale* 2014, 6, 7764–7779.
- (10) Dong, S.; Roman, M. Fluorescently Labeled Cellulose Nano-Crystals for Bioimaging Applications. *J. Am. Chem. Soc.* 2007, 129, 13810–13811.
- (11) Dong, S.; Cho, H. J.; Lee, Y. W.; Roman, M. Synthesis and Cellular Uptake of Folic Acid-Conjugated Cellulose Nano-Crystals for Cancer Targeting. *Biomacromolecules* 2014, 15, 1560–1567.
- (12) Colacino, K. R.; Arena, C. B.; Dong, S.; Roman, M.; Davalos, R. V.; Lee, Y. W. Folate Conjugated Cellulose Nano-Crystals Potentiate Irreversible Electroporation-induced Cytotoxicity for the Selective Treatment of Cancer Cells. *Technol. Cancer Res. Treat.* 2014, DOI: 10.7785/tert.2012.500428.
- (13) Zoppe, J. O.; Ruottinen, V.; Ruotsalainen, J.; Rönkkö, S.; Johansson, L.-S.; Hinkkanen, A.; Jarvinen, K.; Seppälä, J. Synthesis of Cellulose Nano-Crystals Carrying Tyrosine Sulfate Mimetic Ligands and Inhibition of Alphavirus Infection. *Biomacromolecules* 2014, 15, 1534–1542.
- (14) Abitbol, T.; Palermo, A.; Moran-Mirabal, J. M.; Cranston, E. D. Fluorescent Labeling and Characterization of Cellulose Nanocrystals with Varying Charge Contents. *Biomacromolecules* 2013, 14 (9), 3278–3284.
- (15) Navarro, J. R. G.; Conzatti, G.; Yu, Y.; Fall, A. B.; Mathew, R.; Eden, M.; Bergström, L. Multicolor Fluorescent Labeling of Cellulose Nanofibrils by Click Chemistry. *Biomacromolecules* 2015, 16 (4), 1293–1300.
- (16) Grate, J. W.; Mo, K.-F.; Shin, Y.; Vasdekis, A.; Warner, M. G.; Kelly, R. T.; Orr, G.; Hu, D.; Dehoff, K. J.; Brockman, F. J.; Wilkins, M. J. Alexa Fluor-Labeled Fluorescent Cellulose Nanocrystals for Bioimaging Solid Cellulose in Spatially Structured Microenvironments. *Bioconjugate Chem.* 2015, 26 (3), 593–601.
- (17) Dong, S.; Roman, M. Fluorescently Labeled Cellulose Nanocrystals for Bioimaging Applications. *J. Am. Chem. Soc.* 2007, 129 (45), 13810–13811.
- (18) Nielsen, L. J.; Eyley, S.; Thielemans, W.; Aylott, J. W. Dual fluorescent labelling of cellulose nanocrystals for pH sensing. *Chem. Commun.* 2010, 46, 8929–8931.

- (19) Adriani, G.; de Tullio, M. D.; Ferrari, M.; Hussain, F.; Pascazio, G.; Liu, X.; Decuzzi, P. The preferential targeting of the diseased microvasculature by disk-like particles. *Biomaterials* 2012, 33, 5504–5513.
- (20) Kolhar, P.; Anselmo, A. C.; Gupta, V.; Pant, K.; Prabhakarbandian, B.; Ruoslahti, E.; Mitragotri, S. Using shape effects to target antibody-coated nanoparticles to lung and brain endothelium. *Proc. Natl. Acad. Sci. U. S. A.* 2013, 110, 10753–10758.
- (21) Iannazzo, D.; Piperno, A.; Pistone, A.; Grassi, G.; Galvagno, S. Recent advances in carbon nanotubes as delivery systems for anticancer drugs. *Curr. Med. Chem.* 2013, 20, 1333–1354.
- (22) Ananta, J. S.; Godin, B.; Sethi, R.; Moriggi, L.; Liu, X.; Serda, R. E.; Krishnamurthy, R.; Muthupillai, R.; Bolskar, R. D.; Helm, L.; Ferrari, M.; Wilson, L. J.; Decuzzi, P. Geometrical confinement of gadolinium-based contrast agents in nanoporous particles enhances T1 contrast. *Nat. Nanotechnol.* 2010, 5, 815–821.
- (23) Key, J.; Aryal, S.; Gentile, F.; Ananta, J. S.; Zhong, M.; Landis, M. D.; Decuzzi, P. Engineering discoidal polymeric nanoconstructs with enhanced magneto-optical properties for tumor imaging. *Biomaterials* 2013, 34, 5402–5410.
- (24) Arnida, A.; Janatí-Amsbury, M. M.; Ray, A.; Peterson, C. M.; Ghandehari, H. Geometry and surface characteristics of gold nanoparticles influence their biodistribution and uptake by macro-phages. *Eur. J. Pharm. Biopharm.* 2011, 77, 417–423.
- (25) Kraft, J. C.; Freeling, J. P.; Wang, Z.; Ho, R. J. Emerging research and clinical development trends of liposome and lipid nanoparticle drug delivery systems. *J. Pharm. Sci.* 2014, 103, 29–52.
- (26) Ernsting, M. J.; Murakami, M.; Roy, A.; Li, S. D. Factors controlling the pharmacokinetics, biodistribution and intratumoral penetration of nanoparticles. *J. Controlled Release* 2013, 172, 782–794.
- (27) Alexis, F.; Pridgen, E.; Molnar, L. K.; Farokhzad, O. C. Factors affecting the clearance and biodistribution of polymeric nanoparticles. *Mol. Pharmaceutics* 2008, 5, 505–15.
- (28) Decuzzi, P.; Pasqualini, R.; Arap, W.; Ferrari, M. Intravascular Delivery of Particulate Systems: Does Geometry Really Matter? *Pharm. Res.* 2009, 26, 235–43.
- (29) Black, K. C. L.; Wang, Y.; Luehmann, H. P.; Cai, X.; Xing, W.; Pang, B.; Zhao, Y.; Cutler, C. S.; Wang, L. V.; Liu, Y.; Xia, Y. Radioactive  $^{198}\text{Au}$ -Doped Nanostructures with Different Shapes for In Vivo Analyses of Their Biodistribution, Tumor Uptake, and Intra-tumoral Distribution. *ACS Nano* 2014, 8 (5), 4385–4394.
- (30) Liao, W.-Y.; Li, H.-J.; Chang, M.-Y.; Tang, A. C. L.; Hoffman, A. S.; Hsieh, P. C. H. Comprehensive characterizations of nanoparticle biodistribution following systemic injection in mice. *Nanoscale* 2013, 5, 11079–11086.

- (31) Lin, K.; Wu, C.; Chang, J. Advances in synthesis of calcium phosphate crystals with controlled size and shape. *Acta Biomater.* 2014, 10 (10), 4071–4102.
- (32) Martínez Avila, H.; Feldmann, E.-M.; Pleumeekers, M. M.; Nimeskern, L.; Kuo, W.; de Jong, W. C.; Schwarz, S.; Müller, R.; Hendriks, J.; Rotter, N.; van Osch, G. J. V. M.; Stok, K. S.; Gatenholm, P. Novel bilayer bacterial nanocellulose scaffold supports neocartilage formation in vitro and in vivo. *Biomaterials* 2015, 44, 122–133.
- (33) Uludag, H. Bisphosphonates as a Foundation of Drug Delivery to Bone. *Curr. Pharm. Des.* 2002, 8 (21), 1929–1944.
- (34) Heymann, D.; Ory, B.; Gouin, F.; Green, J. R.; Redini, F. Bisphosphonates: new therapeutic agents for the treatment of bone tumors. *Trends Mol. Med.* 2004, 10 (7), 337–343.
- (35) Tenuta, T.; Monopoli, M. P.; Kim, J. A.; Salvati, A.; Dawson, K. A.; Sandin, P.; Lynch, I. Elution of Labile Fluorescent Dye from Nanoparticles during Biological Use. *PLoS One* 2011, 6 (10), e25556.
- (36) Bigini, P.; Previdi, S.; Casarin, E.; Silvestri, D.; Violatto, M. B.; Facchin, S.; Sitia, L.; Rosato, A.; Zuccolotto, G.; Realdon, N.; Fiordaliso, F.; Salmona, M.; Morpurgo, M. In vivo fate of avidin-nucleic acid nanoassemblies as multifunctional diagnostic tools. *ACS Nano* 2014, 8, 175–87.
- (37) Huang, J. L.; Li, C. J.; Gray, D. G. Cellulose. Nano-Crystals Incorporating Fluorescent Methylcoumarin Groups. *ACS Sustainable Chem. Eng.* 2013, 1, 1160–1164.
- (38) Manzoni, C.; Colombo, L.; Bigini, P.; Diana, V.; Cagnotto, A.; Messa, M.; Lupi, M.; Bonetto, V.; Pignataro, M.; Airoidi, C.; Sironi, E.; Williams, A.; Salmona, M. The molecular assembly of amyloid ab controls its neurotoxicity and binding to cellular proteins. *PLoS One* 2011, 6, e24909.
- (39) Manzoni, C.; Colombo, L.; Messa, M.; Cagnotto, A.; Cantu, L.; Del Favero, E.; Salmona, M. Overcoming synthetic  $\alpha\beta$  peptide aging: a new approach to an age-old problem. *Amyloid* 2009, 16, 71–80.
- (40) Sitia, L.; Paoletta, K.; Romano, M.; Violatto, M. B.; Ferrari, R.; Fumagalli, S.; Colombo, L.; Bello, E.; De Simoni, M. G.; D’Incalci, M.; Morbidelli, M.; Erba, E.; Salmona, M.; Moscatelli, D.; Bigini, P. An integrated approach for the selection of polymeric nanoparticles in targeting triple negative breast cancer. *J. Nanopart. Res.* 2014, 16, 2481.
- (41) Bigini, P.; Atzori, C.; Fumagalli, E.; Cagnotto, A.; Barbera, S.; Migheli, A.; Mennini, T. Lack of caspase-dependent apoptosis in spinal motor neurons of the wobbler mouse. *Neurosci. Lett.* 2007, 426, 106–110.
- (42) Hasani, M.; Cranston, E. D.; Westman, G.; Gray, D. G. Cationic surface functionalization of Cellulose Nano-Crystals. *Soft Matter* 2008, 4, 2238–2244.
- (43) Patil, S.; Sandberg, A.; Heckert, E.; Self, W.; Seal, S. Protein adsorption and cellular uptake of cerium oxide nanoparticles as a function of zeta potential. *Biomaterials* 2007, 28, 4600–4607.

- (44) Lundqvist, M.; Stigler, J.; Elia, G.; Lynch, I.; Cedervall, T.; Dawson, K. A. Nanoparticle size and surface properties determine the protein corona with possible implications for biological impacts. *Proc. Natl. Acad. Sci. U. S. A.* 2008, 105, 14265–14270.
- (45) Ten, E.; Ling, C.; Wang, Y.; Srivastava, A.; Dempere, L. A.; Vermerris, W. Lignin nanotubes as vehicles for gene delivery into human cells. *Biomacromolecules* 2014, 15 (1), 327–338.
- (46) He, C.; Hu, Y.; Yin, L.; Tang, C.; Yin, C. Effects of particle size and surface charge on cellular uptake and biodistribution of polymeric nanoparticles. *Biomaterials* 2010, 31, 3657–3666.
- (47) Petros, R. A.; DeSimone, J. M. Strategies in the design of nanoparticles for therapeutic applications. *Nat. Rev. Drug Discovery* 2010, 9, 615–627.
- (48) Mahmoud, K. A.; Mena, J. A.; Male, K. B.; Hrapovic, S.; Kamen, A.; Luong, J. H. Effect of surface charge on the cellular uptake and cytotoxicity of fluorescent labeled Cellulose Nano-Crystals. *ACS Appl. Mater. Interfaces* 2010, 2, 2924–2932.
- (49) Papa, S.; Rossi, F.; Ferrari, R.; Mariani, A.; De Paola, M.; Caron, I.; Fiordaliso, F.; Bisighini, C.; Sammali, E.; Colombo, C.; Gobbi, M.; Canovi, M.; Lucchetti, J.; Peviani, M.; Morbidelli, M.; Forloni, G.; Perale, G.; Moscatelli, D.; Veglianese, P. Selective Nanovector Mediated Treatment of Activated Proinflammatory Microglia/Macro-phages in Spinal Cord Injury. *ACS Nano* 2013, 7 (11), 9881–9895.
- (50) Tsugiyama, H.; Okimura, C.; Mizuno, T.; Iwadate, Y. Electroporation of adherent cells with low sample volumes on a microscope stage. *J. Exp. Biol.* 2013, 216, 3591–3598.
- (51) Gottesman-Davis, A.; Shao, M.; Hirsch, J. C.; Peusner, K. D. Electrophysiological properties of morphologically-identified medial vestibular nucleus neurons projecting to the abducens nucleus in the chick embryo. *Neuroscience* 2011, 172, 494–509.
- (52) Kiessling, F.; Mertens, M. E.; Grimm, J.; Lammers, T. Nanoparticles for Imaging: top or flop? *Radiology* 2014, 273 (1), 10–28.
- (53) Almeida, J. P.; Chen, A. L.; Foster, A.; Drezek, R. In vivo biodistribution of nanoparticles. *Nanomedicine (London, U. K.)* 2011, 6 (5), 815–835.
- (54) Ulrich, S.; Boturyn, D.; Marra, A.; Renaudet, O.; Dumy, P. Oxime Ligation: A Chemoselective Click-Type Reaction for Accessing Multifunctional Biomolecular Constructs. *Chem. - Eur. J.* 2014, 20, 34–41.
- (55) Peri, F.; Cipolla, L.; La Ferla, B.; Dumy, P.; Nicotra, F. A Highly Convergent Approach to O- and N-Linked Glycopeptide analogues. *Glycoconjugate J.* 1999, 16, 399–404.
- (56) Zona, C.; D'Orazio, G.; La Ferla, B. Controlled-Length Efficient Synthesis of Heterobifunctionalized Oligo Ethylene Glycols. *Synlett* 2013, 24, 709–712.

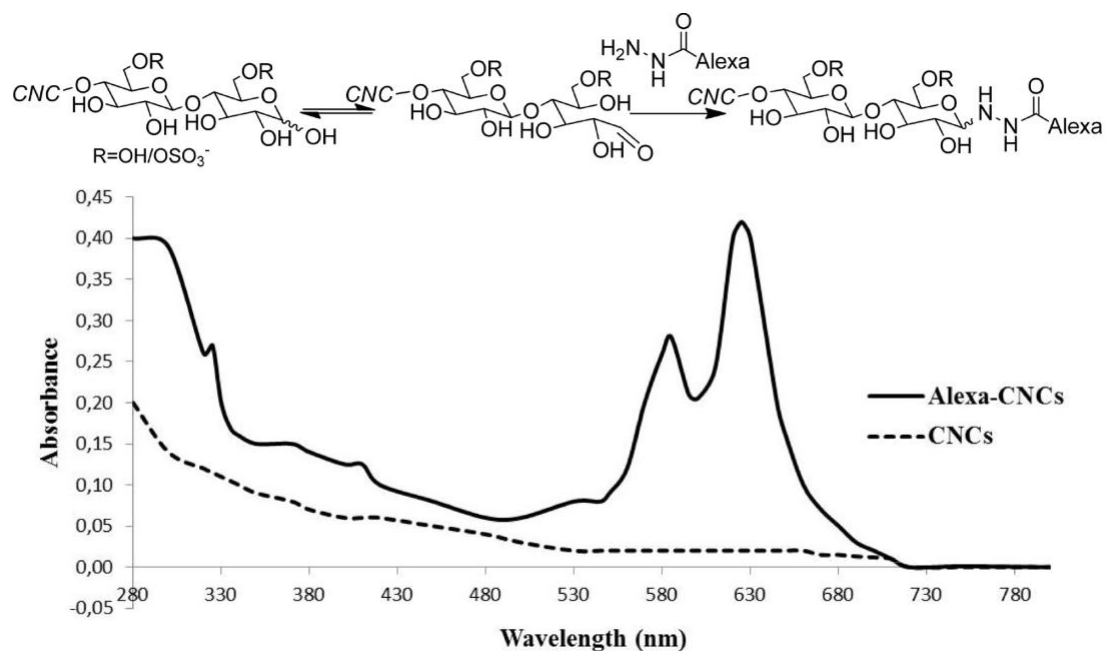


Figure 1. Formation of the CNCs–Alexa Fluor 633 hydrazine conjugates (upper panel). UV–vis spectra of CNCs before and after modification with Alexa Fluor 633 (lower panel).

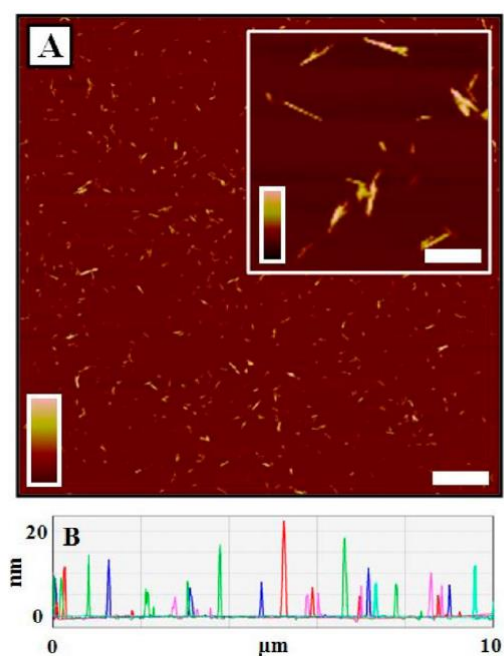


Figure 2. Characterization of CNCs. (A) Representative tapping mode of AFM images as determined by height data of CNCs (Z range:  $-5/+20$  nm). Scale bar,  $2\ \mu\text{m}$ ; inset,  $100\ \text{nm}$ . (B) Height plot profiles obtained along different lines traced on the topographic images.

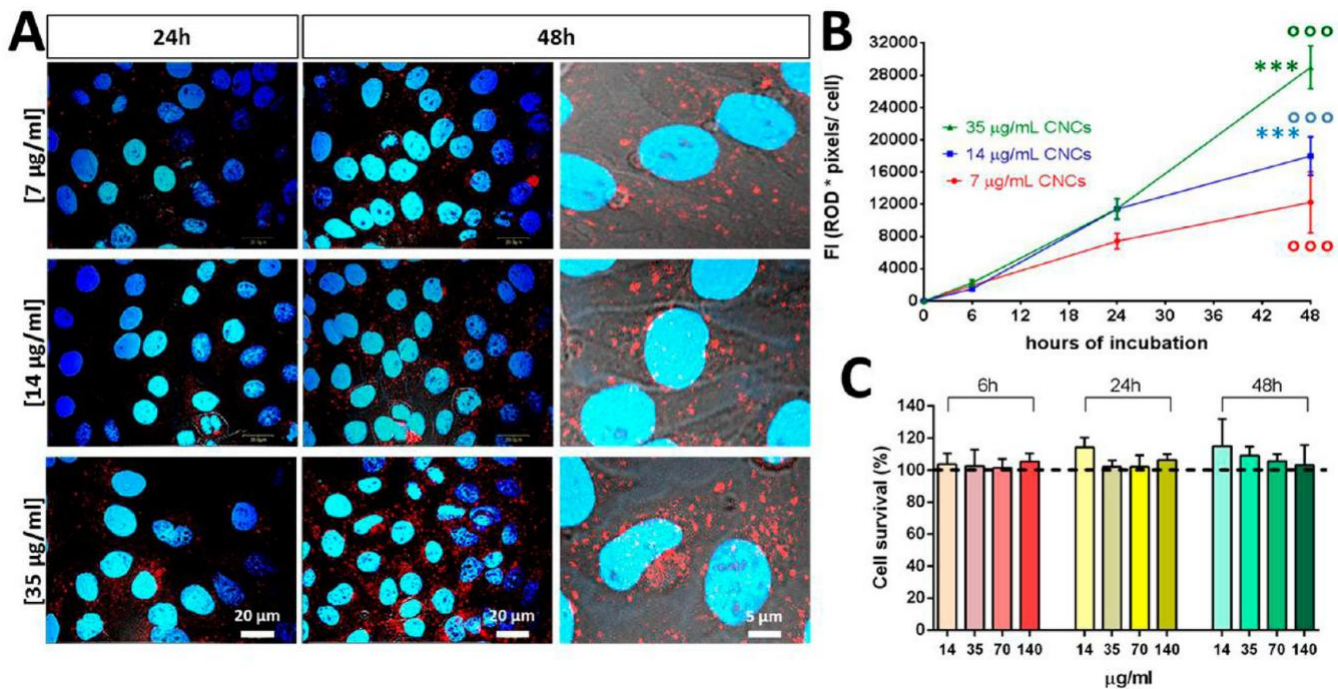
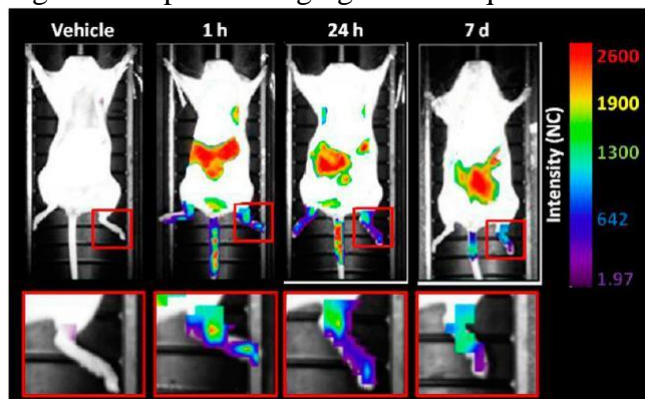


Figure 3. (A) Representative confocal microscopy images showing internalization of different concentrations of CNC-NPs (red signal) in HeLa cells (nuclei, blue signal) after 24 and 48 h of incubation. (B) Diagrams showing the intensity of staining associated with the dye Alexa Fluor 633 in HeLa cells at different time-points and upon three different concentrations. Data are represented as mean  $\pm$  SD; analysis was performed by one-way ANOVA (with Bonferroni post-test). A significant effect of the concentration (\*\*\*)  $p < 0.001$  was observed among the three different groups. A significant effect of incubation time was found for each group (ooo)  $p < 0.001$ . (C) Histogram showing the complete absence of toxicity of CNCs in HeLa cells. Dotted line represents the average number of cells measured in vehicle-treated conditions and normalized at 100 for each time-point. All data were expressed as mean  $\pm$  SD. No significant difference among the different experimental groups was found for any experimental condition.

Figure 4. Optical imaging scans acquired before and at 1 h, 24 h, and 7 d, respectively, after CNCs



intravenous injection (a single dose of 120  $\mu\text{L}$  at a concentration of 35  $\mu\text{g}/\text{mL}$ ). Three different ROIs were processed. They were the abdominal area, the tail, and the distal left hind limb. In the red squares (bottom panels), a higher magnification of the distal hind limb is shown. The fluorescence intensity signal was measured as normalized photon counts (NC) and is shown as a pseudocolor scale bar. The images shown were analyzed with ART OptixOptiview software and are representative of three animals per group.

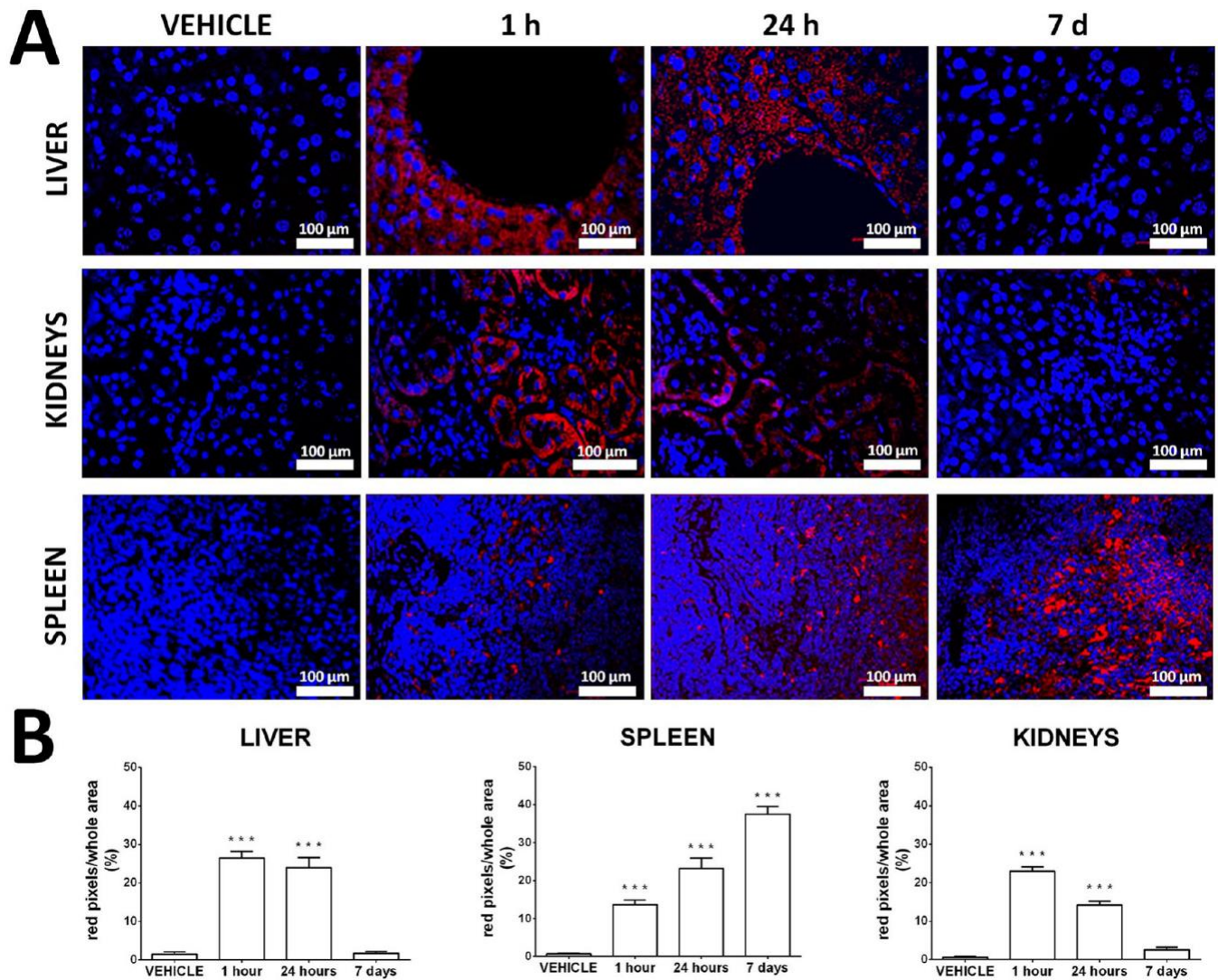


Figure 5. (A) Representative images of liver (upper panels), kidneys (middle panels), and spleen (lower panels) from mice treated with 120  $\mu\text{L}$  of saline solution (first left column) or sacrificed 1 h (second column), 24 h (third column), or 7 days (right column) after intravenous CNCs injection (a single dose of 120  $\mu\text{L}$  at a concentration of 35  $\mu\text{g}/\text{mL}$ ). The blue signal is related to the staining of nuclei with the Hoechst-33258 detectable by exciting the sample by the laser with  $\lambda = 405$  nm. The red staining is associated with Alexa Fluor 633, excited by the laser with  $\lambda = 635$  nm. Scale bars = 100  $\mu\text{m}$ . (B) Quantitative measurement of the fluorescence related to Alexa Fluor 633 (red) in the three organs depicted above. Data are shown as mean  $\pm$  SD and analyzed by one-way ANOVA followed by Bonferroni's test. P-values  $\leq 0.05$  were considered as threshold to establish a statically significant difference between vehicle-treated and CNC-treated mice at different time-points (n = 5 sections and three mice for each experimental group).

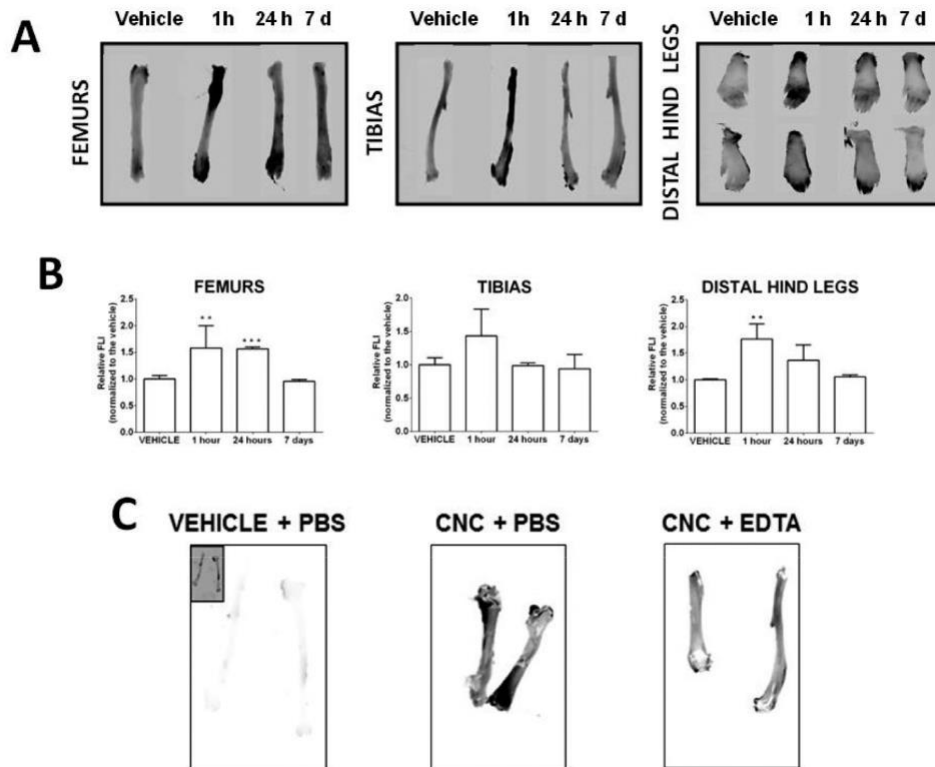


Figure 6. (A) Fluorescence scanning images of femurs, tibias, and distal hind legs analyzed with Thyphoon system ( $\lambda_{exc}$  laser 633). The fluorescence intensity related to CNCs is measured as gray scale, and it could range from a minimum (white) to a maximum (black) signal. (B) Quantitative measurement of fluorescence intensity in samples normalized to the value of each respective vehicle treated mice. Data are presented as mean  $\pm$  SD and analyzed by one-way ANOVA followed by Bonferroni's test. P-values  $\leq 0.05$  were considered as threshold to establish a statically significant difference between vehicle-treated and CNC-treated mice at different time-points ( $n = 5$  for each experimental group). (C) Fluorescence scanning images of femurs and tibias from bones of control mice in PBS (left, in the top corner a higher contrasted picture of the same sample), incubated for 3 h with CNCs (middle), and preincubated in EDTA before CNCs incubation (right).